

# Vortex dynamics around a solid ripple in an oscillatory flow

T. Sand Jespersen<sup>1</sup>, J.Q. Thomassen<sup>1</sup>, A. Andersen<sup>2,a</sup>, and T. Bohr<sup>3</sup>

<sup>1</sup> The Niels Bohr Institute, Blegdamsvej 17, 2100 Copenhagen Ø, Denmark

<sup>2</sup> Cornell University, Department of Theoretical and Applied Mechanics, Ithaca, NY 14853, USA

<sup>3</sup> The Technical University of Denmark, Department of Physics, 2800 Kgs. Lyngby, Denmark

Received 23 October 2003 / Received in final form 6 January 2004

Published online 20 April 2004 – © EDP Sciences, Società Italiana di Fisica, Springer-Verlag 2004

**Abstract.** We investigate the time-dependent flow of water around a solid triangular profile oscillating horizontally in a narrow rectangular container. The flow is quasi two-dimensional and using particle image velocimetry we measure 20 snapshots of the entire velocity field during a period of oscillation. From the velocity measurements we obtain the circulation of the vortices and study the vortex dynamics. The time-dependence of the flow gives rise to the formation of a jet-like flow structure which enhances the vorticity production compared to the time-independent case. We introduce a simple phenomenological model to describe the important dynamical parameters of the flow, i.e., the vortex circulation and the jet velocity. We solve the model analytically without viscous damping and find good agreement between the model predictions and our measurements. Our work adds to the recent effort to understand more complicated flows past sand-ripples and insect wings.

**PACS.** 47.32.Cc Vortex dynamics – 47.32.Ff Separated flows

## 1 Introduction

The formation and dynamics of vortices formed behind solid obstacles in a flow is of great importance in fluid dynamics and has been the subject of many classical studies. The vortex generation in a two-dimensional flow over a solid wedge was investigated by Pullin and Perry [1]. They visualized the formation and motion of the center of the starting vortex formed when accelerating initially motionless water over the wedge. In the present paper we investigate the vortex dynamics in an *oscillatory* flow over a solid triangle, where vortices of alternating vorticity are formed periodically. The vortex formation always takes place on the lee side of the triangle, and the formation process is enhanced by the presence of the “old” vortex which is advected away from the up-wind side. Thus the system is strongly “non-adiabatic” in the sense that results from steady state models are inapplicable. The understanding of time-dependent flows of this type is essential in connection with problems as diverse as, e.g., the formation of sand ripples under oscillatory flows [2–5] and insect flight [6–8]. In fact, this study is inspired by recent work on instabilities in oscillatory “vortex-ripples” in sand. Vortex sand ripples are roughly triangular [2–4], and the dynamics of the separation bubble (the vortex forming on the lee side) is crucial for understanding the changes in sand ripple morphology [5]. The surprisingly sharp crests characteristic of vortex sand ripples arise from the sand

transport caused by the water flow in the recirculation zone, which in turn is intensified by the sharpness of the crests.

Vortex sand ripples are basically two-dimensional since they consist of parallel rows or ridges with a triangular cross section. Thus we have measured the flow around a single “solid” ripple in a geometry which makes the flow approximately two-dimensional. Such a geometry is ideal for measurements by particle image velocimetry (PIV), where snapshots of the entire time-dependent velocity field can be obtained. Measurements using PIV of oscillatory flows over a rippled solid bed have previously been made by Earnshaw and coworkers [9,10]. They obtained the position of the vortex center and the vortex circulation as function of time, and compared the measurements with numerical simulations of a discrete vortex model [10]. The present study is in a completely different parameter regime and we provide detailed measurements of the flow around a single ripple. Furthermore we introduce a new phenomenological model for the vortex dynamics, which we believe will be of interest for future work.

In the following we first describe our experimental technique and discuss the qualitative features of the measured velocity fields. From the measurements we extract the size and strength of the vortex patches (vortices or separation bubbles) forming on the lee side as well as the distribution of the vorticity within them. In addition we obtain the strength of the “jet” which advects the old vortex away and assists in the creation of the new

---

<sup>a</sup> e-mail: apa9@cornell.edu

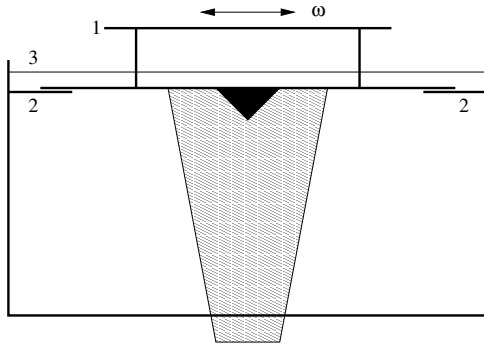


**Fig. 1.** The experimental setup (not to scale). A solid triangle (black) is oscillated horizontally by a motor (not shown). The hatched area is illuminated by a laser sheet used for PIV-measurement. The movable bar (1) supports the triangle and the two small aluminum sheets (2) are designed to minimize the creation of secondary vortices at the container boundary. The surface of the water (3) is always above the flat plate.

vortex. We then introduce a phenomenological model, in the form of a set of coupled ordinary differential equations for the strengths of the vortices and the jet velocity. Finally, we compare the theoretical results with the experimental data and present our conclusions.

## 2 Experimental technique

### 2.1 Experimental setup

Our setup consists of a narrow rectangular Plexiglas container (internal dimensions: 2 cm wide, 35 cm high, and 75 cm long) filled with water, see Figure 1. A Plexiglas triangle (baseline 10 cm and height 5 cm) mounted on a flat rectangular bar is immersed in the water such that it is completely covered. A rail system connects to the bar which is oscillated horizontally with frequency  $f = 0.5$  Hz, i.e., angular frequency  $\omega = 2\pi f = \pi \text{ s}^{-1}$ . The method for creating the oscillatory motion resembles the one used for creating sand-ripples in [5] and the motion is very close to sinusoidal. To ensure minimal disturbance from exposed corners or edges of the moving bar, the bar rests on a 3 mm wide platform milled into the container 3 cm from the top. Two thin aluminum sheets are glued on to extend the platform in the ends. The width of the triangle fits perfectly to the container and water flow between the triangle and the container is negligible.

We present measurements at two different amplitudes of oscillation,  $d_S = 2.5$  cm and  $d_L = 4.6$  cm, which correspond to maximum oscillatory velocities of  $7.9 \text{ cm s}^{-1}$  and  $14.5 \text{ cm s}^{-1}$ , respectively. The Reynolds number for the flow is  $\text{Re} = d^2 \omega / \nu$ , where  $\nu$  is the kinematic viscosity of water. With  $\nu = 0.0089 \text{ cm}^2 \text{ s}^{-1}$  we have  $\text{Re}_S = 2206$  and  $\text{Re}_L = 7469$ , and for both the small and the large amplitude the Reynolds number is therefore intermediate.

The narrow geometry of the container forces the flow to be almost two-dimensional and thus well-suited for PIV

measurements [11]. The PIV laser-sheet is placed vertically as illustrated in Figure 1. The PIV measurement is triggered at a desired phase in the period of oscillation by an optical coupling to the driving mechanism. In the present study the PIV setup was as follows: The two pictures were taken with 10 ms intervals for the large amplitude and with 25 ms intervals for the small amplitude. The images were processed by PIV cross-correlation software employing a 75% overlap of the subfields giving a raw velocity field of 60 by 60 vectors with a spatial resolution of  $0.29 \text{ cm} \times 0.29 \text{ cm}$ .

### 2.2 Data analysis

#### 2.2.1 Validation and averaging of the velocity fields

The raw PIV data were validated in two steps. First we used a global size validation scheme in which very long velocity vectors ( $|\mathbf{u}| > 20 \text{ cm s}^{-1}$ ) attributed to erroneous particle tracking were rejected and replaced by an average of their eight neighboring velocity vectors. Secondly we used a moving average algorithm. For each vector  $\mathbf{u}_i$  in the field we calculated the average  $\mathbf{M}_i$  of its eight neighbors and the difference  $\Delta_i = |\mathbf{M}_i - \mathbf{u}_i|$ . If  $\Delta_i > \alpha \max_i(\Delta_i)$  we replaced  $\mathbf{u}_i$  by  $\mathbf{M}_i$ . For the parameter  $\alpha$  we used the value 0.8. The procedure was repeated three times. Finally an average was made of 10 to 20 velocity fields from the same phase of oscillation. The resulting velocity fields are smooth and the turbulent fluctuations have been averaged out leaving only the large coherent structures.

Figures 2 and 3 show the velocity fields in the 1st half period of the oscillation at the large amplitude. The phase indicated in each panel is chosen such that  $0^\circ$  corresponds to the triangle being at rest furthest to the right and  $90^\circ$  to it moving with maximum velocity toward the left.

#### 2.2.2 Calculation of the vorticity field

In a two-dimensional flow  $\mathbf{u} = (u, v)$  in the  $xy$ -plane the only non-zero component of the vorticity  $\omega = \nabla \times \mathbf{u}$  is in the  $z$ -direction

$$\omega_z = \frac{\partial v}{\partial x} - \frac{\partial u}{\partial y}. \quad (1)$$

We calculate the vorticity fields by differentiating the discrete velocity fields using the *least squares* difference scheme for the points having the four necessary neighbors in the given direction and the *center* difference scheme for points near the triangle or edges of the velocity field where only two neighbors are available. For the line of points closest to the triangle no reliable calculation could be made with this method. These points are shown in gray in the vorticity plots.

The vorticity fields corresponding to each of the measured velocity fields at the large amplitude are shown in Figures 2 and 3 as contour plots of  $\omega_z$  with blue attributed to positive and red to negative vorticity. The same color scale is used for all the plots with the brightest red attributed to points with  $\omega_z \leq -16 \text{ s}^{-1}$ , and points with

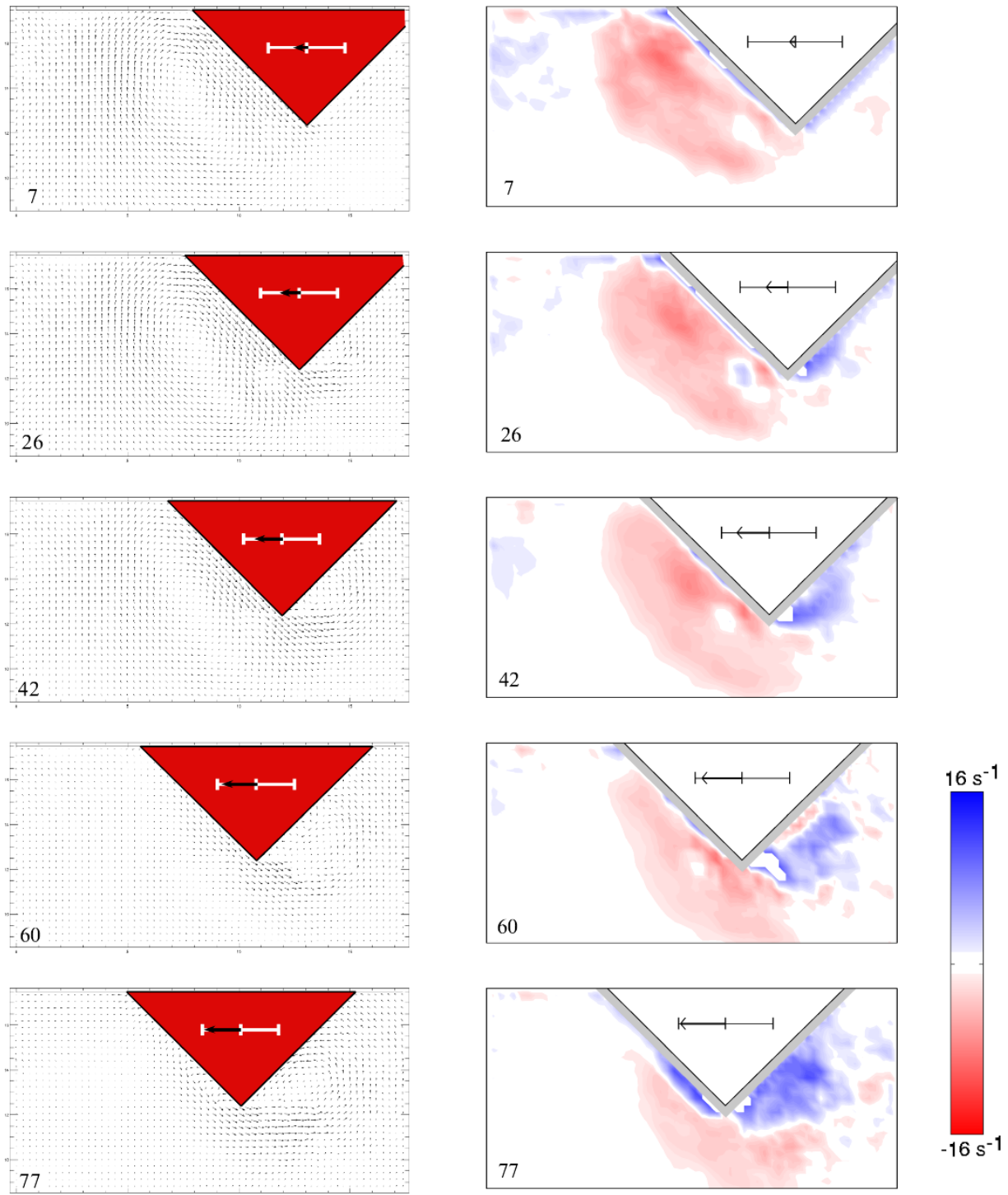


**Fig. 2.** Velocity fields (left) and vorticity fields (right) in the 1st quarter of the period at the large amplitude. The phase in degrees is shown in the lower left corner of each field and in the vorticity plots blue is attributed to positive vorticity and red to negative vorticity. Phase 7°–26°: The strong clockwise vortex to the left is moving down along the triangle, while a large jet, the right part of the vortex, is beginning to move past the crest. Phase 42°–77°: A large anti-clockwise vortex is forming to the right of the triangle. The initial formation and growth is strengthened by the jet originating from the left vortex. This jet is shooting over the tip of the triangle and is so wide that it reaches some way into the fluid below the triangle.

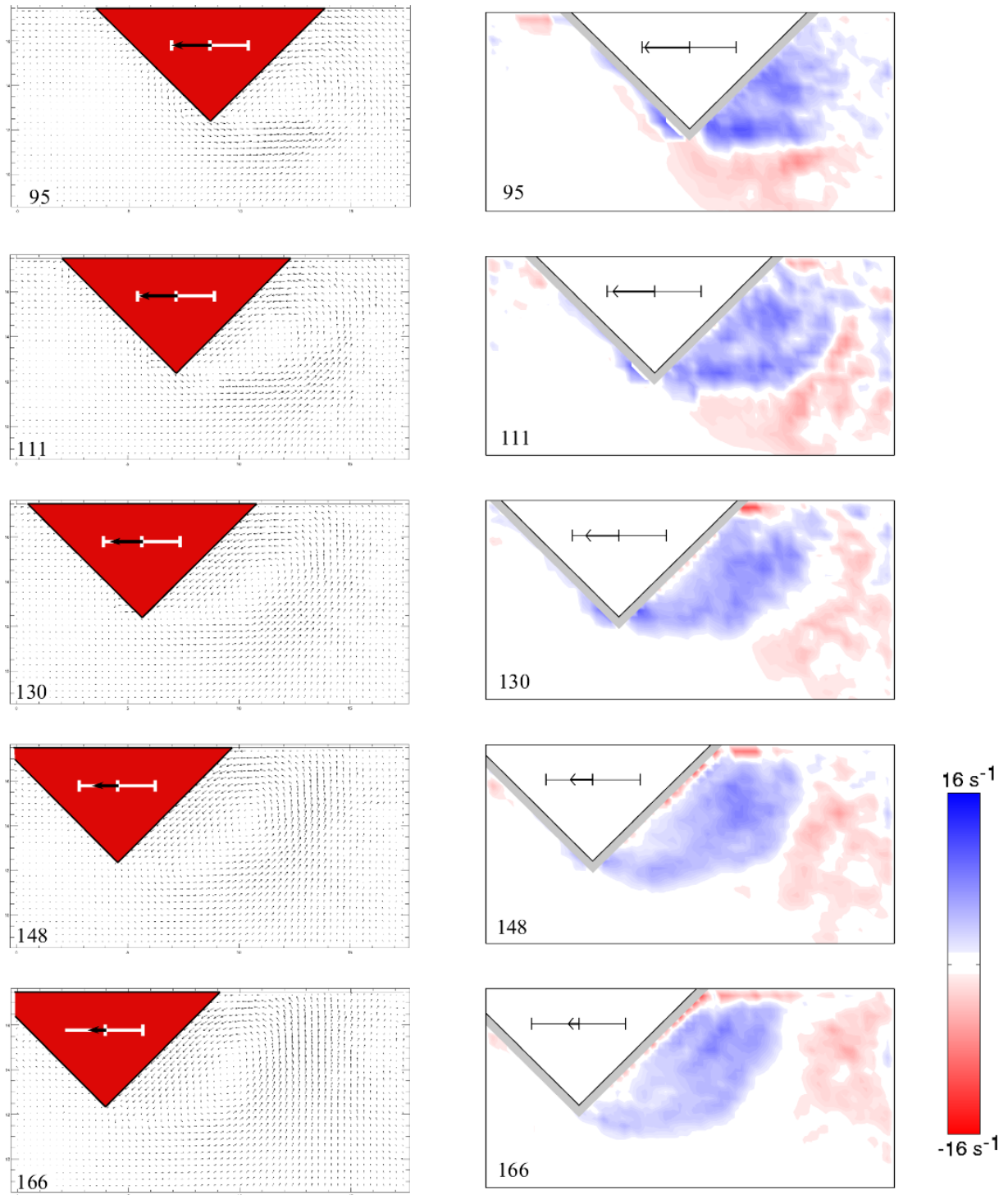


**Fig. 3.** Velocity fields (left) and vorticity fields (right) in the 2nd quarter of the period at the large amplitude. The phase in degrees is shown in the lower left corner of each field and in the vorticity plots blue is attributed to positive vorticity and red to negative vorticity. Phase  $95^{\circ}$ – $166^{\circ}$ : The right vortex grows in size and its center moves upward and away from the triangle. A large jet is formed in the part of the separation zone between the vortex center and the triangle. This jet will generate the growth of the next vortex. The lower part of the separation zone is bounded by an almost horizontal flow starting at the crest. The strength of this flow is determined by the velocity of the triangle, and therefore slows down at the end of the 1st half-period.

$\omega_z \geq 16 \text{ s}^{-1}$  being the brightest shade of blue. For clarity, areas with vorticity around  $0 \text{ s}^{-1}$  are kept white. The plotting routine finds the best continuous contour curves fitting the discrete data. The fields therefore seem continuous, but for all subsequent calculations involving the vorticity we use the underlying discrete field.

### 2.2.3 Calculation of the divergence

In order to check our expectation of a two-dimensional flow, we have calculated the two-dimensional divergence of the velocity field

$$\nabla \cdot \mathbf{u} = \frac{\partial u}{\partial x} + \frac{\partial v}{\partial y}. \quad (2)$$

Since the flow is incompressible the two-dimensional divergence is a measure of the flow velocity in the  $z$ -direction. The sign of the two-dimensional divergence (not shown) varies randomly throughout the flow field without any correlation to the position of the vortices. We thus conclude that there is no systematic error due to flow out of the plane of the laser sheet.

## 3 Quantitative measures

We now discuss certain quantitative measures of the vortices which we determine from the velocity fields. Note that in computing these measures we have used directly the velocity fields shown in Figures 2 and 3 with no additional averaging. Thus the fluctuations in Figures 4–8 are evident. We have not attempted to put in error-bars, but by including an entire period we have made it possible to estimate the fluctuations in most of the images by comparing the two half-strokes which should be identical after sufficient averaging. The quantitative measures will be used to test the validity of the model in Section 4.

### 3.1 Definition of the vortex

In describing the flow it is crucial to have a definition of the vortex. There are two vortices of opposite sign in each field and we define the vortex in the following way: A point in the field belongs to a vortex if the vorticity is larger (smaller) than 20% of the extreme positive (negative) vorticity value in the appropriate field. The cut-off value 20% is chosen as the smallest value which excludes the random vorticity fluctuations in the mean flow from the vortex. With this definition, the vortices coincide nicely with the shaded regions of Figures 2 and 3 except at the very end of the life of the vortex where the vorticity distribution of the vortex flattens, resulting in vortices slightly larger than the regions colored within the color scale chosen for the figures. When this situation occurs the vortex is ill-defined and excluded from further analysis. With this method of identifying the vortices we can now calculate the vortex strength, position, and size.

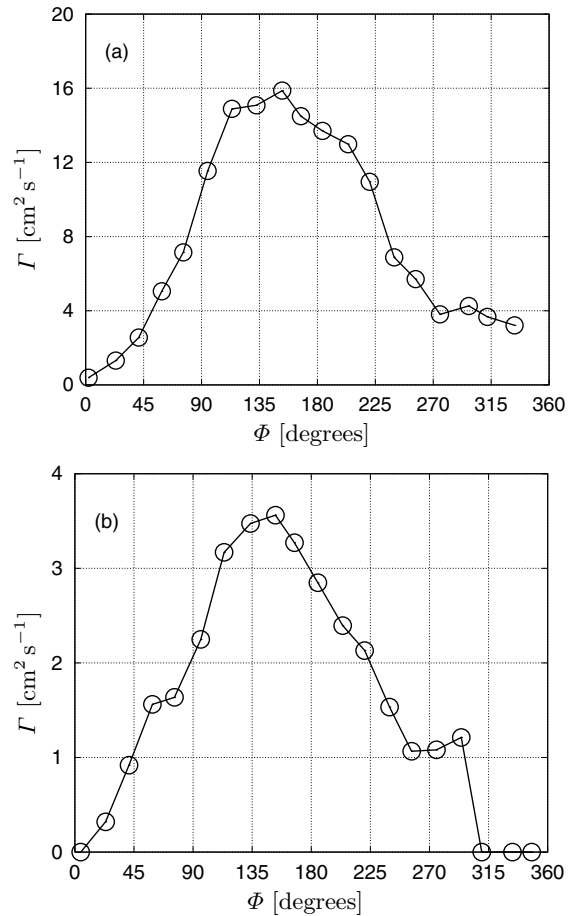


**Fig. 4.** The vortex strength  $\Gamma$  as function of phase  $\Phi$ . (a) the large amplitude and (b) the small amplitude. The three last data points for the small amplitude have been set to zero.

### 3.2 The vortex strength

A numerical integration of the vorticity within the vortex yields the total circulation of the vortex

$$\Gamma = A \sum_{i \in \text{vortex}} \omega_i, \quad (3)$$

where  $A$  is the area of a grid cell. Since the two vortices in a field can be considered as the same vortex shifted by a phase of  $180^\circ$  and with the opposite sign we have data from two full vortex life cycles. By flipping the sign of the negative vortex and shifting the phase appropriately we calculate the average circulation of the two vortices yielding our best estimate of the vortex strength  $\Gamma$ . The results for both oscillation amplitudes as function of the phase,  $\Phi \equiv \omega t$ , are shown in Figure 4. We first consider the results for the large amplitude. The vorticity increases rapidly from  $0 \text{ cm}^2 \text{ s}^{-1}$  when the triangle is at rest to  $\Gamma \approx 15 \text{ cm}^2 \text{ s}^{-1}$  at  $\omega t = 110^\circ$ . From  $\omega t \approx 110^\circ$  until the triangle reverses its direction at  $\omega t = 180^\circ$  the vorticity is almost constant in the range  $15\text{--}16 \text{ cm}^2 \text{ s}^{-1}$ , and not until the flow is reversed at  $\approx 180^\circ\text{--}270^\circ$  do we see a significant decrease of  $\Gamma$ . Care must be taken when considering the last 3–4 data points since the values are strongly dependent on the definition of the vortex. The vortex is strongest

at  $\omega t \approx 155^\circ$  with a value of  $\Gamma_{max}^L \approx 16.0 \text{ cm}^2 \text{ s}^{-1}$ . When we compare the data from the two amplitudes we see a similar qualitative picture although the plateau is less apparent at the small amplitude. The maximum  $\Gamma$  for the small oscillation amplitude is  $\Gamma_{max}^S \approx 3.5 \text{ cm}^2 \text{ s}^{-1}$ .

### 3.3 The vortex size

By counting the number of grid cells in the vortex we find the vortex area as shown in Figure 5. The vortices are quite large with widespread vorticity and the vortices are therefore not intense flow-structures with highly concentrated vorticity. Consider first the large amplitude. The area of the vortex grows concurrently with the buildup of the vortex strength  $\Gamma$ , but the maximum area of  $A_{max}^L \approx 30 \text{ cm}^2$  is not reached until  $\omega t \approx 200^\circ$  which is later in the period than what we found for the maximum value of  $\Gamma$ . There is an obvious plateau between  $\omega t \approx 150^\circ$  and  $\omega t \approx 225^\circ$  where the area of the vortex is close to its maximum value. If we compare the data from the two amplitudes we find the same functional form up until  $\omega t \approx 260^\circ$  where the vortex area for the small amplitude suddenly increases again. This happens because the vorticity in the vortex flattens thereby giving an artificially large area, and this effect is relatively larger with the small amplitude because of smaller values of vorticity in the vortices but relatively larger noise in the field. These last data points should be disregarded when considering the area. With the small amplitude we find that the maximum area is  $A_{max}^S \approx 8 \text{ cm}^2$  which is about four times smaller than  $A_{max}^L$ .

### 3.4 The motion of the vortex center

There are several possible definitions of the center of the vortex. The geometric center (the point around which the fluid is rotating) depends on the choice of reference system (the rest system of the triangle or the laboratory system) and it is therefore not a good definition. The vorticity is a differential quantity and does not change when a constant velocity is added and is therefore better suited as the foundation for a definition. The point of maximum vorticity is problematic as vortex center, since there are often more than one peak within the vortex. Therefore, following [10], we define the center point as a ‘‘center of vorticity’’ in analogy with the center of mass

$$\mathbf{r}_c = \frac{A}{\Gamma} \sum_{i \in \text{vortex}} \omega_i \mathbf{r}_i, \quad (4)$$

where  $A$  is the area of a grid cell. The origin of the reference system is taken to be at the tip of the triangle. Figure 6 shows the paths of the two vortices with respect to the triangle. The vortex is moving along the side of the triangle away from the tip as long as the flow is in the same direction and at some point the direction is reversed and it moves rapidly along the side of the triangle toward the tip. When it passes the tip, the trajectory bends around the new vortex that is being formed on the new lee side of the triangle.

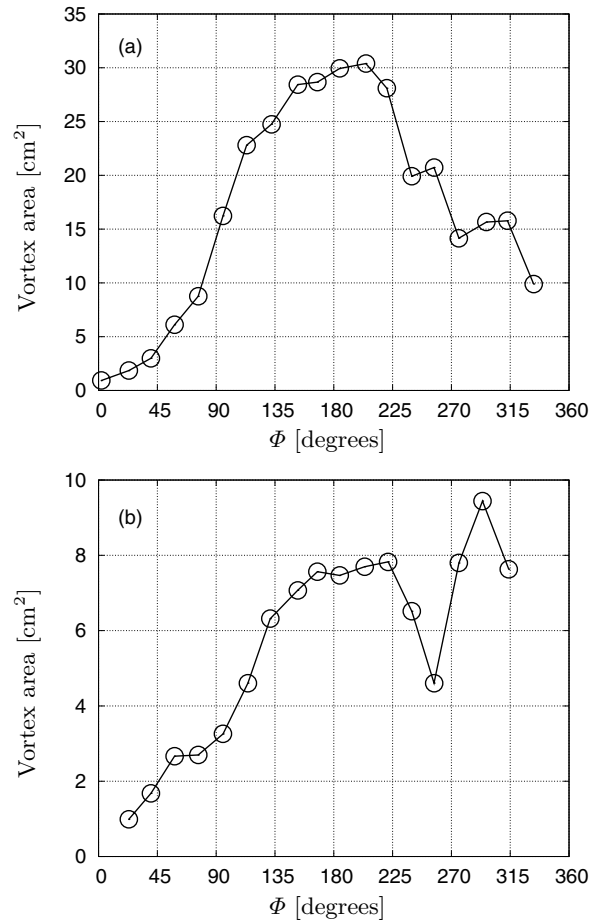


**Fig. 5.** The area of the vortices as defined in Section 3.3. (a) the large amplitude and (b) the small amplitude.

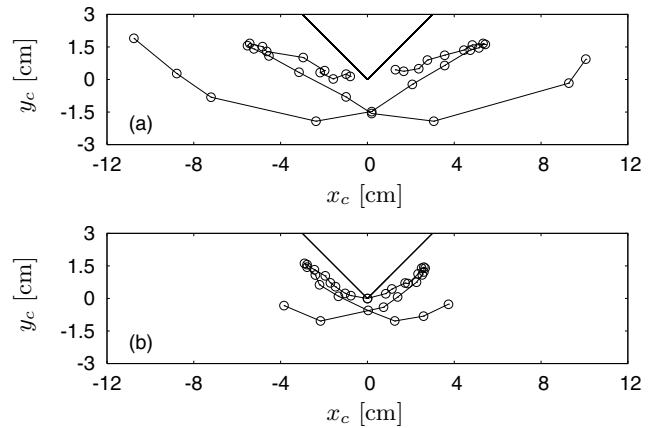


**Fig. 6.** The motion of the vortex center relative to the triangle. (a) at the large amplitude and (b) at the small amplitude.

The center motion is resolved in Figure 7 where the coordinates of the vortex center are shown as a function of phase. For both amplitudes the direction of each center coordinate  $\mathbf{r}_c = (x_c, y_c)$  is reversed at the same instant  $\omega t \approx 155^\circ$  as the strength  $\Gamma$  begins its decline. The non-adiabatic effect, that the vortex reverses direction *before* the triangle does (at  $\omega t = 0^\circ$ ), shows that the flow around the triangle is strongly history dependent. Comparing the

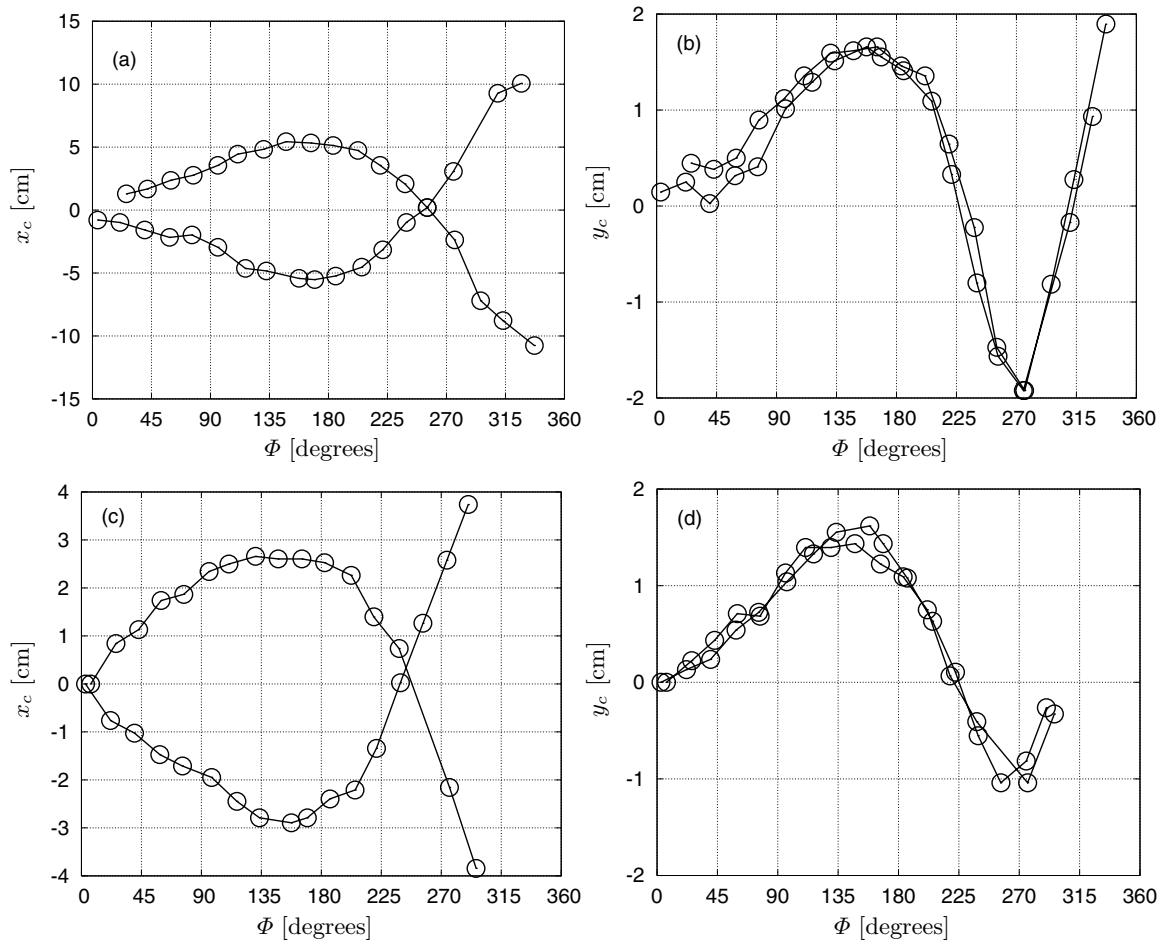


**Fig. 7.** The coordinates  $x_c$  and  $y_c$  of the vortex center for the vortices formed on the left and the right side of the triangle as functions of phase. Figures (a) and (b) are for the large amplitude and figures (c) and (d) are for the small amplitude. The curves for the vortex formed on the left hand side of the triangle are shifted by a phase of  $180^\circ$ .

results from the two amplitudes we see that the vortex reaches the same distance in the  $y$ -direction but twice the distance in the  $x$ -direction when the amplitude is roughly doubled.

### 3.5 Jet velocity

In order to investigate further the increased velocity around the tip (the jet) due to the presence of the vortices we extract the maximal velocity (with respect to the triangle) vertically below the tip of the triangle. This velocity is shown in Figure 8 as a function of phase along with the triangle velocity. For both amplitudes the maximum value of the velocity is about 1.6 times the maximum value of the driving velocity of the triangle, and the maximum is reached at a phase about  $10^\circ$  before the triangle reaches its maximum velocity.

## 4 Phenomenological model

### 4.1 Motivation of the model

The basic variables are the vortex strengths  $\Gamma_+$  and  $\Gamma_-$  on the two sides of the triangle and the velocity  $U$  of the fluid

close to the tip (measured relative to the triangle), which we shall refer to as the “jet velocity”.  $\Gamma_+$  is always positive and  $\Gamma_-$  is always negative. We only keep track of the vorticity until it is advected across the center line. After that it remains zero until the new vorticity production starts, and we can thus only compare with the measured values from Section 3.2 up to this point. The external drive has amplitude  $d$  and the horizontal displacement of the triangle is  $x = d \cos \omega t$ , so that the unperturbed flow velocity around the triangle is  $V_0 = d \omega \sin \omega t$ . We assume that the relevant time scale is  $\omega^{-1}$  and that the flow around the triangle does not depend on the length of the baseline of the triangle and the triangle height, and thus the only relevant length scale is  $d$ . We model the vortex strengths using the following bilinear differential equation expressed in terms of the dimensionless parameters  $A_1, \dots, A_4$ :

$$\begin{aligned} \dot{\Gamma}_+ &= A_1 U^2 \theta(V_0) - A_2 \omega \Gamma_+ \\ &\quad + A_3 d \omega U \theta(-V_0) \theta(\Gamma_+) \end{aligned} \quad (5)$$

$$\begin{aligned} \dot{\Gamma}_- &= -A_1 U^2 \theta(-V_0) - A_2 \omega \Gamma_- \\ &\quad + A_3 d \omega U \theta(V_0) \theta(-\Gamma_-) \end{aligned} \quad (6)$$

$$U = V_0 \left[ 1 - \frac{A_4}{\omega d^2} \theta(V_0) \Gamma_- + \frac{A_4}{\omega d^2} \theta(-V_0) \Gamma_+ \right], \quad (7)$$

where  $\theta$  is the familiar Heaviside step function  $\theta(x) = 0$  for  $x < 0$  and  $\theta(x) = 1$  for  $x > 0$ . The motivation for the terms are the following: In equations (5) and (6), the  $A_1$ -terms express the vorticity production:  $\Gamma_+$  is only produced when  $U > 0$  and  $\Gamma_-$  only when  $U < 0$  (since the square parenthesis in equation (7) is always positive these conditions are equivalent to  $V_0 > 0$  and  $V_0 < 0$ , respectively). Classical estimates of vortex production [12] give  $A_1 = \frac{1}{2}$ . It is however well-known that the actual vorticity produced can be far smaller [13–15]. The classical estimate assumes that the velocity close to the solid surface is near zero, whereas in reality, the vortex which is created generates a velocity of the same order of magnitude and direction as the “free stream” there. In addition, it is not clear which fraction of the available vorticity will actually be entrained behind the solid triangle and become caught up in the separation vortex. In the following we shall thus regard  $A_1$  as a phenomenological parameter.

The  $A_2$ -terms describe exponential damping due to viscosity or turbulent fluctuations. It is always present. The  $A_3$ -terms express the decay of vorticity due to advection. For the vortex formed on the right with  $\Gamma_+ \geq 0$  the  $A_3$ -term in equation (5) is active when the velocity  $U$  around the triangle is negative. The coefficient  $A_3$  is itself positive and since the  $A_3$ -term is proportional to  $U$  it is negative during the half-period when  $\Gamma_+$  decays. Similarly for the  $A_3$ -term in equation (6) which is positive during the half-period when the negative vortex formed on the left side of the triangle decays. Thus the  $A_3$ -term always acts to reduce the absolute value of the vorticity. The  $A_4$ -terms in equation (7) are included since we assume that vorticity *upwind* of the tip enhances the jet. We simply take it to be proportional to the driving velocity and the vorticity present. In reality this term describes a complicated interaction, which depends on the detailed shape and motion of the vortices.

## 4.2 Scaling

We now use dimensionless time  $\tau = \omega t$ , and correspondingly we introduce dimensionless vortex strengths  $y_{\pm}$  such that  $\Gamma_{\pm} = \omega d^2 b y_{\pm}$  and a dimensionless velocity  $u$  such that  $U = \omega d a u$ , where  $a$  and  $b$  are additional dimensionless scaling parameters to be fixed below. In terms of these new variables we obtain

$$\dot{y}_+ = \frac{A_1 a^2}{b} u^2 \theta(V_0) - A_2 y_+ + \frac{A_3 a}{b} u \theta(-V_0) \theta(y_+) \quad (8)$$

$$\dot{y}_- = -\frac{A_1 a^2}{b} u^2 \theta(-V_0) - A_2 y_- + \frac{A_3 a}{b} u \theta(V_0) \theta(-y_-) \quad (9)$$

$$u = \frac{V_0}{\omega d a} [1 - A_4 b \theta(V_0) y_- + A_4 b \theta(-V_0) y_+] , \quad (10)$$

where the dot now means derivative with respect to  $\tau$ , which we denote by  $t$  in the following, since we shall only use the scaled variables. It is natural to take  $a = 1$  because then the driving term has the simple form:  $V_0/\omega a d = \sin t$ .

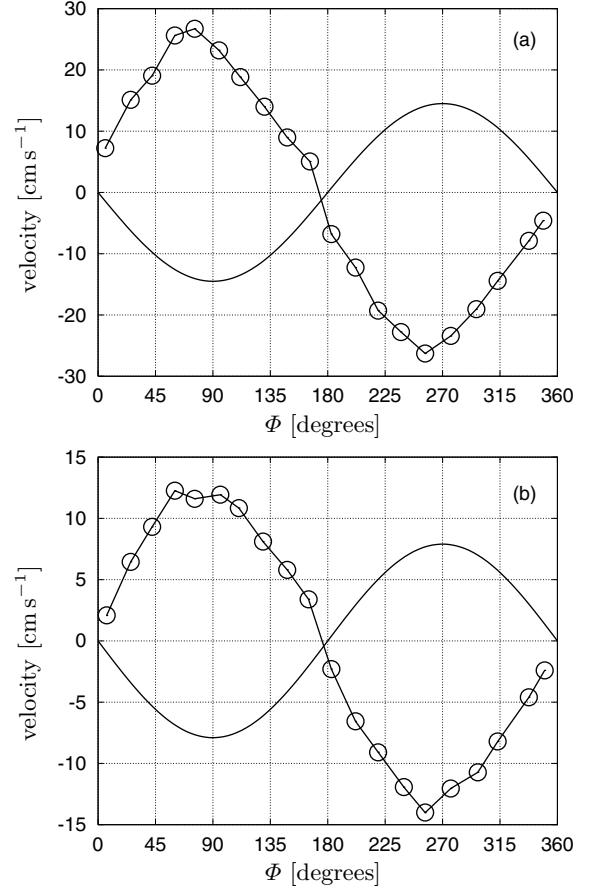


**Fig. 8.** The solid line shows the velocity of the triangle and the solid line with circles shows the jet velocity, i.e., the maximal  $x$ -velocity vertically below the triangle tip. (a) the large amplitude and (b) the small amplitude.

Further, we choose the coefficient  $A_1 \frac{a^2}{b}$  for the vortex production term to be unity and thus  $b = A_1$ . The final form is then

$$\dot{y}_+ = u^2 \theta(\sin t) - b_2 y_+ + b_3 u \theta(-\sin t) \theta(y_+) \quad (11)$$

$$\dot{y}_- = -u^2 \theta(-\sin t) - b_2 y_- + b_3 u \theta(\sin t) \theta(-y_-) \quad (12)$$

$$u = \sin t [1 - b_4 \theta(\sin t) y_- + b_4 \theta(-\sin t) y_+] , \quad (13)$$

where we have

$$b_2 = A_2, \quad b_3 = \frac{A_3}{A_1}, \quad b_4 = A_4 A_1 . \quad (14)$$

## 4.3 Numerical solution

Typical numerical solutions are shown in Figure 9. Interesting periodic solutions exist only within a small parameter region. If the vorticity production is small  $U$  and  $V_0$  become almost identical. If, on the other hand, the vorticity production becomes too large, the vorticity cannot be swept away by the jet and it can increase without bound. It seems that the interesting states – those that look like the experiments – are very close to the “critical point”

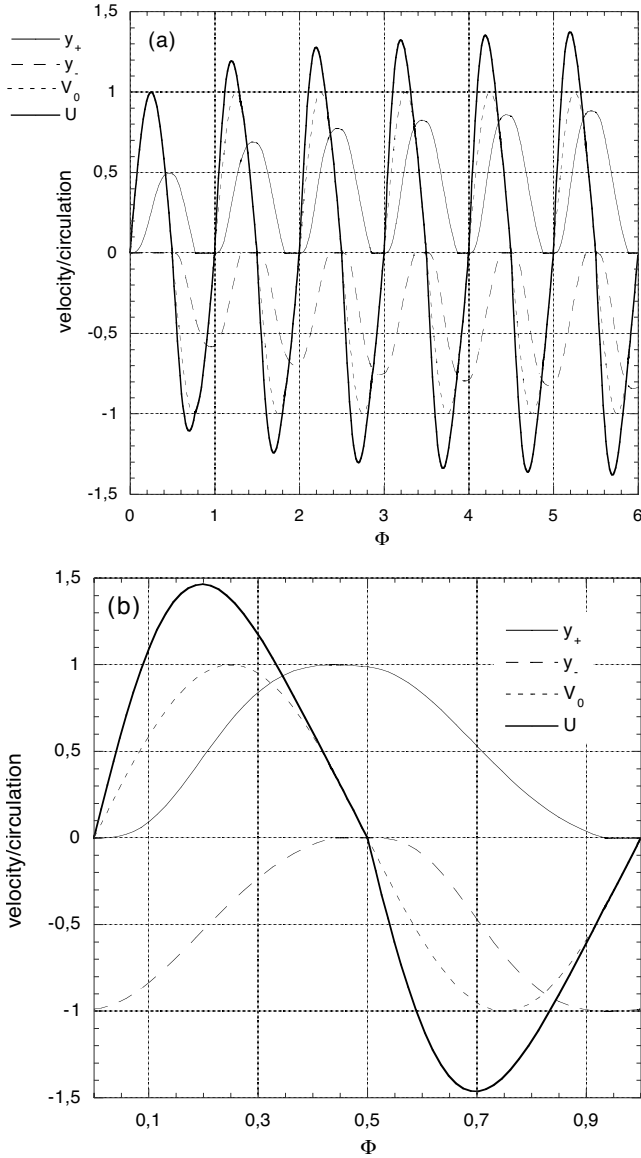


**Fig. 9.** Solution of equations (11–13). Figure (a) initial cycles starting from rest and figure (b) final periodic state. The parameters are  $b_2 = 0.3/2\pi \approx 0.0484$ ,  $b_3 = 1.0$  and  $b_4 = 2.15/2\pi \approx 0.34$ . The circulations  $y_{\pm}$  have been scaled by 2.968 to give a maximal value of 1.

where the vorticity diverges. In other words, the experimentally relevant states seem to correspond to particular combinations of the parameters  $b_2 \dots b_4$ . In this sense, it behaves like a self-resonating system [16]. In Section 4.4 we shall find the allowed combinations of parameters in the undamped case, where the model can be solved exactly.

#### 4.4 Analytic solution for $b_2 = 0$

We now discuss analytically the special case  $b_2 = 0$ , i.e., no damping due to viscosity (there is still damping due to

advection represented by  $b_3$ ). We get

$$\dot{y}_+ = u^2 \theta(\sin t) + b_3 u \theta(-\sin t) \theta(y_+) \quad (15)$$

$$\dot{y}_- = -u^2 \theta(-\sin t) + b_3 u \theta(\sin t) \theta(-y_-) \quad (16)$$

$$u = \sin t [1 - b_4 \theta(\sin t) y_- + b_4 \theta(-\sin t) y_+] \quad (17)$$

##### 4.4.1 General analytic solution

To find the solution for an arbitrary period  $[2n\pi, 2(n+1)\pi]$ , it has to be split into four parts  $[2n\pi, t^*]$ ,  $[t^*, (2n+1)\pi]$ ,  $[(2n+1)\pi, \tilde{t}^*]$  and  $[\tilde{t}^*, 2(n+1)\pi]$ .

The solution for  $t \in [2n\pi, (2n+1)\pi]$  is, first for  $y_-$ :

$$y_-(t) = \begin{cases} \frac{1}{\alpha} (1 - u^* e^{-\beta(1-\cos t)}) & \text{for } 2n\pi < t < t^* \\ 0 & \text{for } t^* < t < (2n+1)\pi, \end{cases} \quad (18)$$

where for convenience  $\alpha = b_4$  and  $\beta = b_3 b_4$ . The constant  $u^* = 1 - \alpha y^*$ , where we define  $y^* = y_-(2n\pi)$ . If  $y_-(t)$  becomes zero somewhere in the interval, at  $t = t^*$ , it will remain so. The solution for  $y_-$  in the remaining interval is

$$y_-(t) = \begin{cases} -(\tilde{u}^*)^2 \int_{(2n+1)\pi}^t e^{-2\beta(1+\cos t')} \sin^2 t' dt' & \text{for } (2n+1)\pi < t < \tilde{t}^* \\ y_-(\tilde{t}^*) - \frac{1}{2}(t - \tilde{t}^*) + \frac{1}{4}(\sin 2t - \sin 2\tilde{t}^*) & \text{for } \tilde{t}^* < t < 2(n+1)\pi \end{cases} \quad (19)$$

where  $\tilde{t}^*$  will be defined later.

For  $u$  we get

$$u(t) = \begin{cases} u^* e^{-\beta(1-\cos t)} \sin t & \text{for } 2n\pi < t < t^* \\ \sin t & \text{for } t^* < t < (2n+1)\pi \\ \tilde{u}^* e^{-\beta(1+\cos t)} \sin t & \text{for } (2n+1)\pi < t < \tilde{t}^* \\ \sin t & \text{for } \tilde{t}^* < t < 2(n+1)\pi. \end{cases} \quad (20)$$

Finally, we get for  $y_+$ :

$$y_+(t) = (u^*)^2 \int_{2n\pi}^t e^{-2\beta(1-\cos t')} \sin^2 t' dt', \quad (21)$$

which is valid for  $t < t^*$ . For  $t \in [t^*, (2n+1)\pi]$  we have

$$\begin{aligned} y_+(t) &= y_+(t^*) + \int_{t^*}^t \sin^2 t' dt' \\ &= y_+(t^*) + \frac{1}{2}(t - t^*) - \frac{1}{4}(\sin 2t - \sin 2t^*). \end{aligned} \quad (22)$$

Similarly we get for  $t \in [(2n+1)\pi, 2(n+1)\pi]$

$$y_+(t) = \begin{cases} -\frac{1}{\alpha} (1 - \tilde{u}^* e^{-\beta(1+\cos t)}) & \text{for } (2n+1)\pi < t < \tilde{t}^* \\ 0 & \text{for } \tilde{t}^* < t < 2(n+1)\pi \end{cases} \quad (23)$$

where  $\tilde{u}^* = 1 + \alpha \tilde{y}^*$  and  $\tilde{y}^* = y_+(2n\pi + \pi)$ .

#### 4.4.2 Integral equation for $t^*$ in the periodic state

In the periodic state we have  $\tilde{y}^* = -y^*$ ,  $\tilde{u}^* = u^*$  and  $\tilde{t}^* = t^* + \pi$ . Note the symmetry of the periodic state:

$$u(t + \pi) = -u(t) \quad (24)$$

$$y_-(t + \pi) = -y_+(t). \quad (25)$$

As can be seen  $u$  is not differentiable at  $t = n\pi$  in the periodic state. In fact  $u'(\pi_-) = -1$  and  $u'(\pi_+) = -u^*$ . The existence of a  $t^*$  where all the vorticity has been “blown” away is necessary for attaining a periodic state, since otherwise vorticity will accumulate and lead to divergent solutions. For a  $t^*$  to exist we must have

$$1 - \cos t^* = \frac{1}{\beta} \ln(u^*). \quad (26)$$

The existence of a periodic state is governed by the following integral equation for  $y^*$  (or  $u^*$ ) and  $t^*$  obtained using equation (25)

$$\frac{u^* - 1}{\alpha} = (u^*)^2 e^{-2\beta} \int_0^{t^*} e^{2\beta \cos t} \sin^2 t dt + \frac{1}{2}(\pi - t^*) + \frac{1}{4} \sin 2t^*. \quad (27)$$

This equation together with the relation (26) can be combined to give one final equation for  $t^*$ :

$$e^{\beta(1 - \cos t^*)} - 1 = \alpha \left[ \int_0^{t^*} e^{2\beta(\cos t - \cos t^*)} \sin^2 t dt + \frac{1}{2}(\pi - t^*) + \frac{1}{4} \sin 2t^* \right]. \quad (28)$$

To have physical solutions we must have  $\pi/2 < t^* < \pi$ . The upper limit  $t^* = \pi$  gives

$$\begin{aligned} \alpha_+ &= \frac{1 - e^{-2\beta}}{\int_0^\pi e^{2\beta \cos t} \sin^2 t dt} \\ &= \frac{2\beta (1 - e^{-2\beta})}{\pi I_1(2\beta)} \\ &= \frac{2}{\pi} \frac{1 - e^{-2\beta}}{I_0(2\beta) - I_2(2\beta)}, \end{aligned} \quad (29)$$

where  $I_0$ ,  $I_1$ , and  $I_2$  are Bessel functions. The interesting solutions, in the sense that they are resonant, i.e., give large amplitudes, have  $t^*$  close to  $\pi$  (at least within the interval  $3\pi/4 < t^* < \pi$ ). Figure 10 shows the two lines  $\alpha = \alpha(\beta)$  corresponding to,  $t^* = \pi$  (solid line) and  $t^* = 3\pi/4$  (dashed line), respectively. The meaningful solutions occur between these two curves for  $\beta < \beta^* \approx 0.385$ , where they cross.

Figure 11 shows a typical numerical solution for the periodic state at  $\beta = 0.25$  and  $\alpha = 0.2387$  (and no damping), which as can be seen in Figure 12 lies in the allowed region of the phase diagram. It is well represented by the analytical solution in Section 4.4.

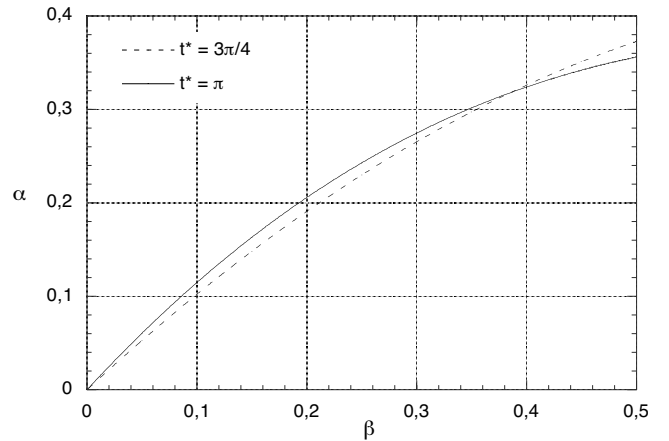


**Fig. 10.** Phase diagram in the variables  $\beta = b_3 b_4$  and  $\alpha = b_4$ . The solid line shows  $t^* = \pi$  and the dashed line  $t^* = 3\pi/4$ . The meaningful solutions occur between these curves before the lines cross at  $\beta = \beta^*$ .

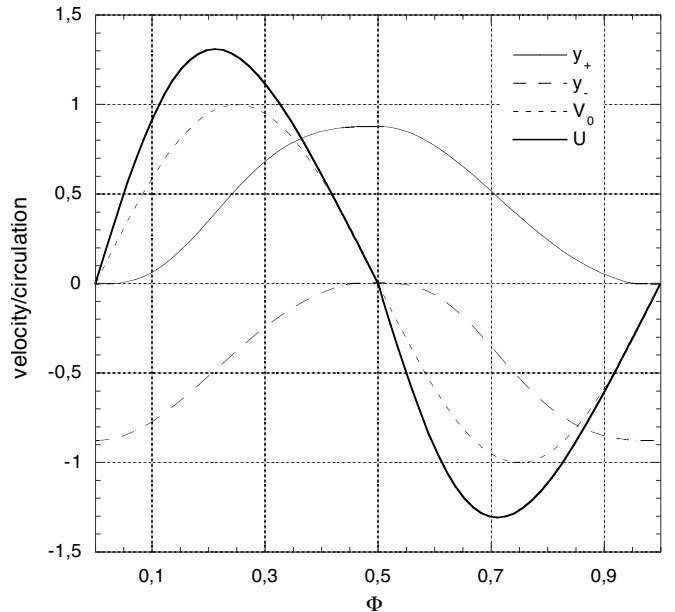


**Fig. 11.** Solution of equations (11–13) with  $b_2 = 0$ . Final periodic state with  $\beta = 0.25$  and  $\alpha = 0.2387$ .

#### 4.5 Maximal value of $u$

Experimentally, the maximal value of  $u$  is  $u_{max} \approx 1.6$ . The maximal value can be found from equation (20). The function  $\sin(t) \exp(\beta \cos t)$  has a maximum when  $\cos t - \beta(\sin^2 t) = \beta \cos^2 t + \cos t - \beta = 0$  or

$$\cos t = \frac{1}{2\beta} \left( -1 \pm \sqrt{1 + 4\beta^2} \right), \quad (30)$$

which means that the phase  $\phi$  where  $u$  is maximal is

$$\phi = \arccos \left[ \frac{1}{2\beta} \left( -1 \pm \sqrt{1 + 4\beta^2} \right) \right], \quad (31)$$

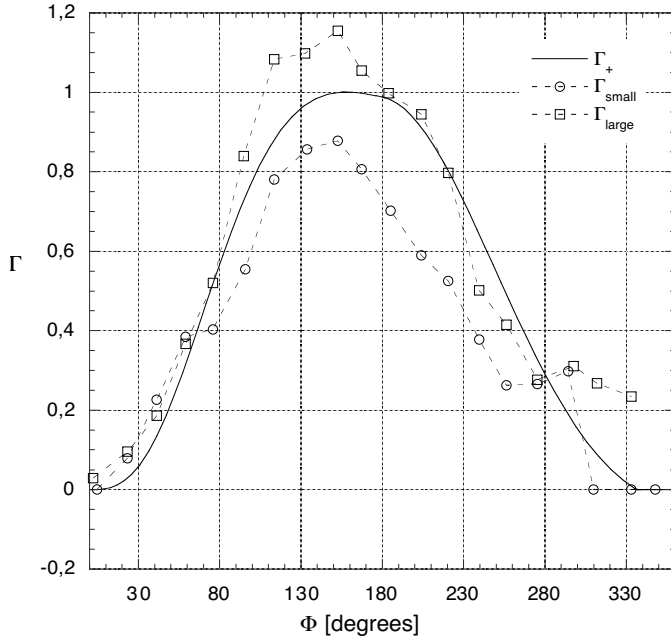


**Fig. 12.** The theoretical and the experimental circulation as function of time. The experimental data sets have been scaled as described in the text.

with one solution (choosing the plus sign)  $\phi \in [0, \pi/2]$ . Then

$$\begin{aligned} u_{max} &= u^* e^{-\beta(1-\cos\phi)} \sin\phi \\ &= u^* \frac{1}{\sqrt{2}\beta} \sqrt{(\sqrt{1+4\beta^2}-1)} e^{(\sqrt{1+4\beta^2}-2\beta-1)/2}. \end{aligned} \quad (32)$$

#### 4.6 Comparison with experiment

In the experiment we have  $\omega = \pi s^{-1}$  and the two amplitudes  $d_S = 2.5$  cm and  $d_L = 4.6$  cm. The maximal measured vortex strengths are  $\Gamma_{max}^S = 3.5$  cm<sup>2</sup>s<sup>-1</sup> and  $\Gamma_{max}^L = 16.0$  cm<sup>2</sup>s<sup>-1</sup>. In the comparison we use the scaling from Section 4.2, i.e.,  $\Gamma_{\pm} = A_1 \omega d^2 y_{\pm}$ . In the state corresponding to the numerical solution in Figure 9, we have maximal values of  $y_{\pm}$  around 3 and we find that  $A_1 \approx 0.07$  (see also the discussion of  $A_1$  in Sect. 4.1). In Figure 12 we show a comparison between the circulations from the experiment and the numerical solution corresponding to Figure 9. We have scaled the theoretical circulation as in Figure 9 (to make the maximum unity) and we have scaled the experimental circulations by factors 13.73 cm<sup>2</sup>s<sup>-1</sup> and 4.06 cm<sup>2</sup>s<sup>-1</sup> with the ratio  $(d_L/d_S)^2$  according to the scaling assumptions of Section 4.2. It is seen that the general form and the position of the maximum are well reproduced.

In Figure 13 we compare the velocities. Here the experimental velocities (Fig. 8) are scaled by  $\omega d$ , i.e., by 14.45 cm s<sup>-1</sup> and 7.86 cm s<sup>-1</sup>, respectively. Again the similarity between experiment and theory is surprisingly good, considering the very simple character of the latter.

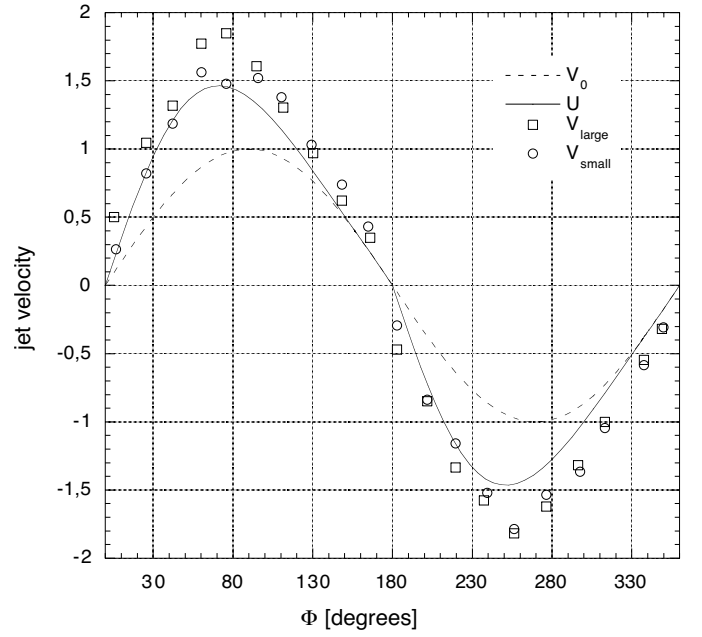


**Fig. 13.** The theoretical and the experimental curves for the jet-velocity. The parameters of the model are as in Figure 9. The experimental data sets have been scaled as described in the text.

## 5 Discussion and conclusions

The generation of vortices, or separation zones, around periodically moving solid structures, is a surprisingly violent process. In particular, the initiation of a vortex depends strongly on the localized jet which is formed slightly after the triangle has reversed its direction of motion. We have developed a simple phenomenological model for the generation of the vortices and their interaction with the jet, which can be solved exactly in the limit of no viscous damping and which compares favorably with our experimental results. Our results emphasize the non-adiabatic and history dependent character of the formation of separation zones in time-dependent flows, which means that this process can not be captured by steady state calculations.

The phenomenology described and modeled in this paper is important for the development of quantitative models of the formation and evolution of “vortex ripples” in the sand under oscillating water flow. In particular it is important for understanding the instabilities, which occur when the oscillatory drive changes [5], leading, e.g., to the creation of new ripples in the troughs between the old ones that already exist. Here the strength and size of the separation vortex determines the position and growth of the new ripple. In this context, it would be of great interest to extend our model to two dimensions, and include the instabilities which occur in the transverse direction and deform the cylindrical separation vortex.

Another problem for which our results might be relevant is insect flight, i.e., the generation of lift and thrust by flapping wings at intermediate Reynolds numbers [6–8]. Here the nature and strength of the separation vortices

(so-called leading edge vortices) is of primary importance, and non-adiabatic effects are known to be large.

We are very thankful to Knud Erik Meyer and Nicolas Pedersen for making the PIV equipment at the Department of Fluid Mechanics at the Technical University of Denmark available to us and for their crucial help in carrying out the experiment. A. A. acknowledges the support from AFOSR Grant No. F49620-01-1-0530 and ONR Grant No. N00014-01-1-0688 granted to Z. Jane Wang.

## References

1. D.I. Pullin, A.E. Perry, *J. Fluid Mech.* **97**, 239 (1980)
2. H. Ayrton, *Proc. Roy. Soc. A* **84**, 285 (1910)
3. R.A. Bagnold, *Proc. Roy. Soc. A* **187**, 1 (1946)
4. A. Stegner, J.E. Wesfreid, *Phys. Rev. E* **60**, R3487 (1999)
5. J.L. Hansen, M. van Hecke, A. Haaning, C. Ellegaard, K.H. Andersen, T. Bohr, T. Sams, *Nature* **410**, 324 (2001); J.L. Hansen, M. van Hecke, C. Ellegaard, K.H. Andersen, T. Bohr, A. Haaning, T. Sams, *Phys. Rev. Lett.* **87**, 204301 (2001)
6. C.P. Ellington, C. van den Berg, A.P. Willmott, A.L.R. Thomas, *Nature* **384**, 626 (1996)
7. M.H. Dickinson, F.-O. Lehmann, S.P. Sane, *Science* **284**, 1954 (1999)
8. Z.J. Wang, *Phys. Rev. Lett.* **85**, 2216 (2000)
9. H.C. Earnshaw, T. Bruce, C.A. Greated, W.J. Easson, *Proc. of the 24th Int. Conf. of Coastal Engineering*, p. 1975 (1994)
10. H.C. Earnshaw, C.A. Greated, *Exp. Fluids* **25**, 265 (1998)
11. M. Raffel, C.E. Willert, J. Kompenhans, *Particle Image Velocimetry* (Springer-Verlag, Berlin, Heidelberg, 1998)
12. L. Prandtl, O.G. Tietjens, *Fundamentals of Hydro- and Aeromechanics* (Dover, New York, 1957)
13. N. Didden, *J. Applied Math. Phys. (ZAMP)* **30**, 101 (1979)
14. M. Gharib, E. Rambod, K. Shariff, *J. Fluid Mech.* **360**, 121 (1998)
15. M. Rosenfeld, E. Rambod, M. Gharib, *J. Fluid Mech.* **376**, 297 (1998)
16. A. Boudaoud, Y. Couder, M. Ben Amar, *Phys. Rev. Lett.* **82**, 3847 (1999)

Copyright of European Physical Journal B -- Condensed Matter is the property of Kluwer Academic Publishing / Academic and its content may not be copied or emailed to multiple sites or posted to a listserv without the copyright holder's express written permission. However, users may print, download, or email articles for individual use.